JACS
JOURNAL OF THE AMERICAN CHEMICAL SOCIETY
pubs.acs.org/JACS
Article

Fast Li^+ Conduction Mechanism and Interfacial Chemistry of a NASICON/Polymer Composite Electrolyte

Nan Wu,◇ Po-Hsiu Chien,◇ Yutao Li,* Andrei Dolocan, Henghui Xu, Biyi Xu, Nicholas S. Grundish, Haibo Jin, Yan-Yan Hu, and John B. Goodenough*

Cite This: J. Am. Chem. Soc. 2020, 142, 2497−2505

Read Online

ACCESS | Metrics & More | Article Recommendations | Supporting Information

ABSTRACT: The unclear Li^+ local environment and Li^+ conduction mechanism in solid polymer electrolytes, especially in a ceramic/polymer composite electrolyte, hinder the design and development of a new composite electrolyte. Moreover, both the low room-temperature Li^+ conductivity and large interfacial resistance with a metallic lithium anode of a polymer membrane limit its application below a relatively high temperature. Here we have identified the Li^+ distribution and Li^+ transport mechanism in a composite polymer electrolyte by investigating a new solid poly(ethylene oxide) (PEO)-based NASICON−$LiZr_2(PO_4)_3$ composite with ^7Li relaxation time and $^6Li \rightarrow {}^7Li$ trace-exchange NMR measurements. The Li^+ population of the two local environments in the composite electrolytes depends on the Li-salt concentration and the amount of ceramic filler. A composite electrolyte with a $[EO]/[Li^+]$ ratio $n = 10$ and 25 wt % LZP filler has a high Li^+ conductivity of 1.2×10^{-4} S cm^{-1} at 30 °C and a low activation energy owing to the additional Li^+ in the mobile A2 environment. Moreover, an in situ formed solid electrolyte interphase layer from the reaction between $LiZr_2(PO_4)_3$ and a metallic lithium anode stabilized the Li/composite-electrolyte interface and reduced the interfacial resistance, which provided a symmetric Li/Li cell and all-solid-state $Li/LiFePO_4$ and $Li/LiNi_{0.8}Co_{0.1}Mn_{0.1}O_2$ cells a good cycling performance at 40 °C.

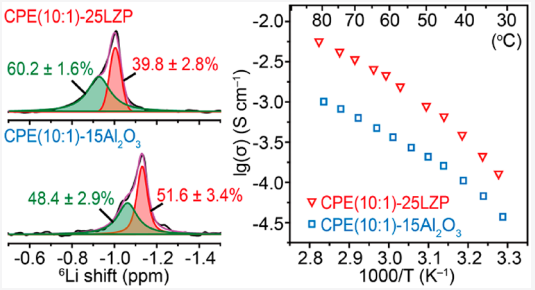

INTRODUCTION

Solid electrolytes with high Li^+ conductivity, small resistance across the electrolyte/electrode interface, and a large electrochemical window may improve the safety and energy density of all-solid-state Li-metal batteries.[1,2] Some oxides (e.g., garnet $Li_{6.5}La_3Zr_{1.5}Ta_{0.5}O_{12}$)[3−5] and sulfide electrolytes (e.g., argyrodite Li_6PS_5Cl)[6−8] have high Li^+ conductivities above 10^{-3} S cm^{-1} at 25 °C. However, these electrolytes are either unstable on contact with a metallic lithium anode or have a large interfacial resistance with different electrodes, and the all-solid-state Li-metal batteries with these electrolytes are short-circuited at an applied current density above 0.3 mA cm^{-2} because of their poor wettability by lithium metal.[9,10] Compared with the inorganic solid electrolytes, the flexible poly(ethylene oxide) (PEO)-based polymer electrolytes show better contact and stability with a Li-metal anode, which reduces the Li/polymer-electrolyte interfacial resistance.[11−14] However, these solid polymer electrolytes have a low Li^+ conductivity of 10^{-6} S cm^{-1} at 25 °C, which increases the operating temperature of PEO-based all-solid-state Li-metal batteries to above 60 °C. Moreover, the small Li^+ transference number, $t_{Li+} \approx 0.2$, in a PEO-based electrolyte also results in a large concentration overpotential polarization during cell charge/discharge; the capacity of the cell decreases to zero at higher current densities.[15−17] PEO and PEO−lithium salts (LiX) crystallize in the form of spherulites at temperatures below 50 °C to form PEO and Li^+-rich phases (e.g., PEO_6−LiX); some Li^+-conducting PEO−LiX electrolytes remain amorphous because of the plasticizing effect of the lithium salts.[18,19] The compositional inhomogeneity of PEO−LiX electrolyte causes a large local current density at a Li-metal-anode/PEO interface, which short circuits the cell at current densities above 0.2 mA cm^{-2}; lithium dendrite growth cannot be suppressed by the PEO−LiX membrane, even at working temperatures above 50 °C owing to its degraded mechanical strength.[20]

Adding a second ceramic phase, including Li^+ insulating oxides (e.g., Al_2O_3/TiO_2)[21] and oxide/sulfide Li^+ conductors (e.g., garnet $Li_7La_3Zr_2O_{12}$ and perovskite $Li_{0.33}La_{0.56}TiO_3$),[22−27] as a filler to the polymer membrane is a useful strategy to improve Li^+ conductivity of the composite polymer electrolyte by (1) the reduction of polymer crystallization, (2) a possible increase of Li^+ transport on the polymer/filler interface, and (3) a possible participation of Li ions from the Li^+-conducting fillers. Moreover, the introduction of these ceramic fillers increases the mechanical strength

Received: November 13, 2019
Published: January 13, 2020

https://dx.doi.org/10.1021/jacs.9b12233
J. Am. Chem. Soc. 2020, 142, 2497−2505

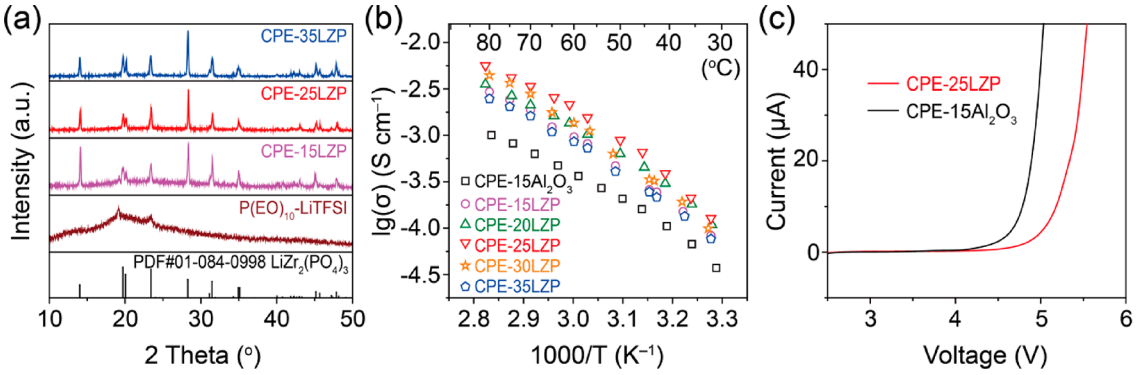

Figure 1. Characterization of the CPE−LZP membrane ([EO]/[Li] ratio n = 10). (a) XRD patterns, (b) Arrhenius plots of the ionic conductivities, (c) linear sweep voltammetry curves. The thickness of composite polymer electrolytes employed in this work is 200 μm.

and the thermal stability of the polymer electrolytes. The Li^+-insulating ceramic fillers such as nano-sized Al_2O_3/TiO_2 powders with large surface area increased Li^+ conductivity of the PEO membrane by 1 order of magnitude; however, a low Li^+ conductivity and small Li^+ transference number limit the commercialization of the polymer electrolyte. The Li^+-conducting garnet is not stable in air and is prone to forming Li_2CO_3/LiOH on its surface, which blocks Li^+ transfer across the PEO/garnet interphase; perovskite $Li_{0.33}La_{0.56}TiO_3$ is easily reduced below 2 V vs Li^+/Li^0.[28,29] Although the conductivity and cycling performance of the all-solid-state Li-metal batteries with different composite electrolytes have been investigated by many research groups,[30,31] the Li^+ local environment and Li^+ conduction mechanism of the solid polymer electrolytes has yet to be thoroughly investigated, especially for the polymer/Li^+-conducting filler composite electrolytes. Therefore, it is still urgent to explore (1) new ceramic fillers that have a strong interaction with the polymer−LiX to improve the Li^+ conductivity and can form a uniform interface with the metallic lithium anode to homogenize the current density at the interface and (2) the Li^+ conduction mechanism of the composite polymer electrolyte.

Here we employed ^{7}Li relaxation time and $^6Li \rightarrow {}^7Li$ trace-exchange nuclear magnetic resonance (NMR) measurements to investigate the Li^+ distribution and Li^+ conduction mechanism of a composite polymer electrolyte by comparing three different PEO−LiTFSI composite electrolytes: without any filler (CPE), PEO−LiTFSI−Al_2O_3 composite electrolyte (CPE−Al_2O_3), and a new PEO−LiTFSI−NASICON−$LiZr_2(PO_4)_3$ (CPE−LZP). $LiZr_2(PO_4)_3$ (LZP) is stable above 5 V and has a bulk Li^+ conductivity of 3.0×10^{-4} S cm^{-1} at 25 °C; the strong P−O bond of the phosphate group in $LiZr_2(PO_4)_3$ increases its chemical stability in air.[32] Two different Li^+ positions are found in all composite polymers, and the Li^+ distribution in the composites depends on the ceramic fillers and the lithium salt concentration. The LZP filler improves the Li^+ conductivity of the polymer electrolyte to 1.2×10^{-4} S cm^{-1} at 30 °C by increasing the concentration and disorder of more mobile Li^+ ions. Moreover, the reaction product Li_3P phase of CPE−LZP on contact with lithium metal is wet by the metallic lithium anode, which reduces the Li-metal anode/polymer membrane interfacial resistance and improves the cycling stability of a symmetric Li/Li cell. All-solid-state Li-metal batteries with $LiFePO_4$ and $LiNi_{0.8}Mn_{0.1}Co_{0.1}O_2$ cathodes showed a high Coulombic efficiency and a long cycle life at 40 °C.

RESULTS AND DISCUSSION

Li^+ Transport of the CPE−LZP Electrolyte. NASICON $LiZr_2(PO_4)_3$ (LZP) prepared by solid-state reaction has a rhombohedral structure and a bulk Li^+ conductivity of 3.0×10^{-4} S cm^{-1} at 25 °C (Figure S1a). Raman spectroscopy of the $LiZr_2(PO_4)_3$ (Figure S1b) does not indicate any presence of a Li_2CO_3 Li^+-blocking layer, which would normally manifest itself as a peak at 1080 cm^{-1} in the spectrum. This observation confirms the stability of $LiZr_2(PO_4)_3$ in air with the strong P−O bond enhancing its chemical stability in comparison with other solid electrolytes. The flexible composite LZP in PEO membrane prepared by a solution-cast method is very dense, and the $LiZr_2(PO_4)_3$ particles with an average size of 15 μm are uniformly distributed in the membrane (Figure S3a). Figure 1a and Figure S2a show the XRD results of the composite CPE−LZP membrane with and without $LiZr_2(PO_4)_3$. The two peaks at 20°and 25° in the PEO−LiTFSI membrane (CPE) are from crystalline PEO, and the broad peak from 15° to 30° originates from an amorphous CPE phase; two small PEO peaks still remain in the CPE−LZP membrane with 15 and 20 wt % LZP. The XRD result of CPE−LZP confirms that $LiZr_2(PO_4)_3$ is stable with PEO−LiTFSI, and the disappearance of the crystalline PEO peak in the CPE−xLZP ($x \geq 25$) membrane indicated that $LiZr_2(PO_4)_3$ acts as a solid plasticizer to increase the amorphous component of the polymer, which improves the Li^+ transfer in the PEO by releasing more free segments of the polymer chains.

The nonlinear Arrhenius plots of the ionic conductivities of the CPE−LZP membranes with different amounts of LZP powders (CPE−xLZP, x is the weight percent of LZP powders) are shown in Figure 1b; all the curves follow a Vogel−Tamman−Fulcher (VTF) behavior from 30 to 80 °C, indicating that the major component of the CPE−LZP membrane is amorphous.[33] The composite membranes with more segmental motion at high temperatures showed higher Li^+ conductivities. The membrane with 25 wt % $LiZr_2(PO_4)_3$ (CPE−25LZP) has a low electronic conductivity of 9.0×10^{-10} S cm^{-1} at 25 °C (Figure S2b) and the highest Li^+-conductivity of 1.2×10^{-4} and 2.1×10^{-3} S cm^{-1} at 30 and 60 °C, respectively. The composite membranes with 15−35 wt % $LiZr_2(PO_4)_3$ showed higher Li^+ conductivities than a PEO−LiTFSI membrane with nano-Al_2O_3 particles (CPE−15Al_2O_3) even at temperatures above the melting point of PEO where the polymer membrane is 100% amorphous. The CPE−25LZP membrane has a much higher Li^+ transference number $t_{Li+} \approx$

https://dx.doi.org/10.1021/jacs.9b12233
J. Am. Chem. Soc. 2020, 142, 2497−2505

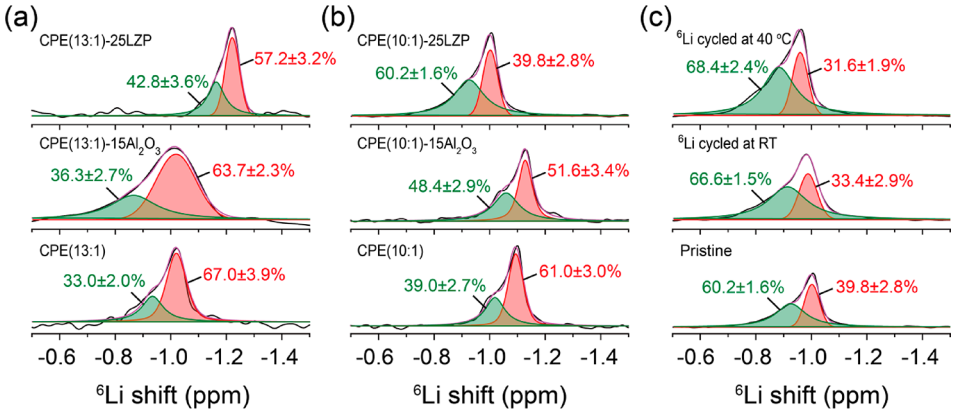

Figure 2. Solid-state ^{6}Li MAS NMR spectra of composite electrolytes studied in this work. (a) PEO_{13}–LiTFSI (CPE (13:1)), PEO_{13}–LiTFSI–15 wt % Al_2O_3 (CPE (13:1)–15Al_2O_3), and PEO_{13}–LiTFSI–25 wt % LZP (CPE (13:1)–25LZP). (b) PEO_{10}–LiTFSI (CPE (10:1)), $P(EO)_{10}$–LiTFSI–15 wt % Al_2O_3 (CPE (10:1)–15Al_2O_3), and PEO_{10}–LiTFSI–25 wt % LZP (CPE (10:1)–25LZP). (c) PEO_{10}–LiTFSI–25 wt % LZP (CPE (10:1)–25LZP), PEO_{10}–LiTFSI–25 wt % LZP cycled with ^{6}Li electrodes at room temperature (middle), and PEO_{10}–LiTFSI–25 wt % LZP cycled with ^{6}Li electrodes at 40 °C (top).

0.36 (Figure S4a) than a CPE–15Al_2O_3 membrane and a PEO-based polymer membrane with garnet ceramic fillers.[16,34,35] These results and the residual crystalline PEO phase in the CPE–25LZP membrane indicate that the degree of PEO crystallization as well as the interaction between the $LiZr_2(PO_4)_3$ particle surface and PEO–LiTFSI influence the Li^+ transfer inside the composite polymer; the Li^+ in the bulk $LiZr_2(PO_4)_3$ may also contribute to the Li^+ transfer of the polymer. Moreover, a CPE–25LZP membrane showed better electrochemical stability than that of CPE at higher voltages (Figure 1c). The interaction between LZP and the polar PEO can influence the electron energy level of PEO to hinder its decomposition above 4 V.[36] Moreover, the Li-salt was reported to decompose before the oxidation of PEO;[35] the stability of the composite electrolyte should be related to the stability of the LiTFSI salt. The higher Li^+ transference number in the composite electrolyte also indicates that LZP stabilizes the $TFSI^-$ anions at high voltages.[35] The FTIR spectra of the composite electrolytes with and without LZP powders further confirmed the LZP–polymer electrolyte interaction (Figure S4b). The peak at 745 cm^{-1} in the FTIR spectra corresponding to the ion-paired signal[37] reduced by 5.6% when 25 wt % LZP was added into the polymer electrolyte (CPE (10:1)). The interaction between LZP and $TFSI^-$ anions limits the movement of $TFSI^-$ anions and frees more Li^+ for Li^+ transport, which can increase the stability of LiTFSI at high voltage. Additionally, since LZP is stable above 5 V,[32] adding 25 wt % of LZP to the composite increases the stability of the composite electrolyte.

The composite electrolytes with different $[EO]/[Li^+]$ ratios (8:1, 10:1, 13:1, and 20:1) and 25 wt % LZP were tested to study the influence of the LiTFSI concentration on the Li^+ conductivity of the composite electrolytes. The XRD and EIS results of these composite membranes are shown in Figure S5. The Li^+ conductivity of the composite electrolyte increases and the mechanical strength decreases with increasing LiTFSI concentration. The composite electrolyte with a $[EO]/[Li^+]$ ratio of 20:1 has a low Li^+ conductivity of 3.0×10^{-6} S cm^{-1} at 30 °C owing to the crystallization of PEO and the low concentration of Li salt. The membrane with an $[EO]/[Li^+]$ ratio of 8:1 showed an improvement in Li^+ conductivity (1.3×10^{-4} S cm^{-1}) at 30 °C but poor mechanical strength compared to the membrane with a $[EO]/[Li^+]$ ratio of 10:1. Moreover, a crystalline phase with a $[EO]/[Li^+]$ ratio of 6:1 formed because of the high Li-salt concentration (Figure S5a). The peak at 745 cm^{-1} related to the ion-pairing in the FTIR spectrum (Figure S6b) increased by 10% when the $[EO]/[Li^+]$ ratio was increased from 10:1 to 8:1. This result indicates that the excess of LiTFSI exists in an ion-paired form rather than being disassociated. As a result, the CPE(8:1)–25LZP and the CPE(10:1)–25LZP membranes present comparable Li^+ conductivity. Additionally, the activation energy of the composite electrolyte decreases as the $[EO]/[Li^+]$ ratio increases from 20:1 to 10:1 (Table S1). Based on its balance of having good conductivity as well as suitable mechanical strength for battery fabrication, the composite polymer electrolyte with $[EO]/[Li^+]$ ratio of 10:1 was selected for battery testing.

Li^+ Local Environment and Conduction Mechanism of the CPE–LZP Electrolyte. Identifying the Li^+ environments and their roles in Li^+ transport is critical to the development of composite electrolytes. Figure 2a shows the ^{6}Li MAS NMR spectra of the composite membrane with different fillers, and all these membranes have the same $[EO]/[Li]$ ratio (n = 13). The ^{6}Li resonances appear at −1.02 ppm in $P(EO)_{13}$–LiTFSI, −1.02 ppm in $P(EO)_{13}$–LiTFSI–15Al_2O_3, and −1.25 ppm in $P(EO)_{13}$–LiTFSI–25LZP. The significantly broad ^{6}Li signal in the $P(EO)_{13}$–LiTFSI–15Al_2O_3 membrane indicates that both the content of amorphous phase and the segmental motions of active chains in the $P(EO)_{13}$–LiTFSI matrix were enhanced by the addition of Al_2O_3 with an average particle size of 5.8 nm.[38] The ^{6}Li LiTFSI signal of $P(EO)_{13}$–LiTFSI–25LZP membrane became narrower and shifted to a higher frequency. The shifting up-field of ^{6}Li LiTFSI resonance in $P(EO)_{13}$–LiTFSI–25LZP implies a weakened PEO–Li^+ interaction;[39] the sharper line-shape suggests that the broadening of the LiTFSI signal caused by anisotropic Li local environments is noticeably averaged out by faster Li^+ motions. Hence, Li^+ released from LiTFSI become more mobile, which is well-supported by the ^{7}Li spin-lattice relaxation time (T_1, Table S2). The ^{7}Li T_1 times are slightly reduced from 0.59 s in $P(EO)_{13}$–LiTFSI to 0.54 s in $P(EO)_{13}$–LiTFSI–15Al_2O_3, and to 0.49 s in $P(EO)_{13}$–LiTFSI–25LZP. In general, a higher Li^+ mobility gives rise to a shorter T_1 time before the correlation time, τ_c (the mean residence time between two successive jumps), passes through the T_1 minimum according to the BPP

https://dx.doi.org/10.1021/jacs.9b12233
J. Am. Chem. Soc. 2020, 142, 2497–2505

model.[40] Therefore, the decreased T_1 times positively correlate with the Li^+ conductivity of these composites. It should be noted that no ^6Li signal of LZP is found in $P(EO)_{13}$−LiTFSI−25LZP, which could be attributed to the low dose of LZP and the small lithium concentration of LZP.

Detailed analysis of the asymmetric peaks of the NMR signal in Figure 2a shows that the overall line-shape is composed of two Li^+ environments. The right peak (A1) amounts to 67% ± 3.9% of total integral and is assigned to the Li^+ (from LiTFSI) that is closely bound to EO units in PEO. The left peak (A2), which is 33% ± 2.0% of the total integral, is associated with Li^+ experiencing local disorder and weakened Li^+-O_{PEO} interactions. This finding is consistent with Greenbaum's work[41] showing that Li^+ in such an environment chemically resembles free Li ions as the chemical shift moves toward zero ppm. Comparison of the ^6Li MAS NMR spectra in Figure 2a shows that more Li^+ migrates from regions near PEO to the disordered environments as Al_2O_3 and LZP fillers are added into the $P(EO)_{13}$−LiTFSI matrix. These findings together with the ^7Li spin-lattice relaxation times (T_1) lead to the hypothesis that Li^+ in disordered environments are more mobile; thus, higher ionic conductivities are expected for composites with a higher abundance of Li^+ in disordered environments.

In order to test this hypothesis, three composites (without inorganic filler, with Al_2O_3, and with LZP) having a high concentration of LiTFSI, that is, [EO]/[Li] ratio n = 10, were prepared, and their ^6Li MAS NMR spectra are shown in Figure 2b. Two obvious changes are observed. First, the fraction of the disordered Li^+ environment (left peak) has notably increased. Second, narrower line shapes are formed in $P(EO)_{10}$−LiTFSI and $P(EO)_{10}$−LiTFSI−15Al_2O_3 composites compared to the composites with an [EO]/[Li] ratio n = 13. The left peak increases in $P(EO)_{10}$−LiTFSI with no fillers by 6% of the total integral over the composite with no filler and an [EO]/[Li] ratio n = 13, suggesting the tendency to form a disordered Li^+ environment increases with the concentration of LiTFSI. This trend of an increased percentage of total integral for disordered Li^+ environments is retained after Al_2O_3 is added (12.1% increase). The disordered Li^+ environments account for 60.2% of the total integral when LZP serves as the inorganic filler in $P(EO)_{10}$−LiTFSI. The ^6Li MAS NMR spectrum of the CPE-25LZP with a [EO]/[Li^+] ratio n = 8 is shown in Figure S6a; the higher dose of LiTFSI results in a higher fraction of Li^+ in the more mobile A2 environment (Figure S6a). Approximately 18% more Li^+ is observed in A2 for the CPE(10:1)−25LZP and CPE(8:1)−25LZP membranes than the CPE(13:1)−25LZP. Thus, the improvement in Li^+ conductivity (Figure S5b) for both the CPE(10:1)−25LZP and CPE(8:1)−25LZP is attributed to the higher Li^+ population of A2. The shorter ^7Li T_1 time (Table S2) of the composite electrolytes with a [EO]/[Li^+] ratio n = 8 and n = 10 than that of the composite electrolyte with a [EO]/[Li^+] ratio n = 13 indicates that Li^+ motion is faster if more LiTFSI is present. These results reconcile the observed narrower line shape with the improvement in Li^+ conductivity.

Based on the difference in chemical shifts between A1 and A2 environments as well as published results,[41,42] Li^+ in A1 can be viewed as solvated Li^+, which is spatially close to H_{EO} in the $-CH_2CH_2-$ carbon chain in PEO. Li^+ in A2, however, is presumably linked to a less restricted, that is, weaker Columbic interaction, space that promotes a higher degree of freedom for dissociated Li^+ to move. Therefore, a further Li^+-H_{EO} distance is expected in A2. This assumption can be validated with $^1H-^6Li$ cross-polarization (CP), which explores the strength of $^1H-^6Li$ dipolar coupling that is dependent on the distance between two nuclei. In addition, variable-temperature (−30 to 80 °C) ^7Li NMR can offer another insight into ion dynamics by detecting the change in line shape. This information can potentially confirm which Li^+ environment is the contributing factor to increasing the overall ionic conductivity in composite polymer electrolytes. These proposed measurements, which are out of scope in this work, can be pursued in future research.

The higher Li^+ conductivity of CPE−25LZP than that of CPE agrees well with the higher fraction of the A2 signal, which may be related to the surface of the LZP particles. The coordinated unsaturated Li^+ on the micro-sized LZP particle surface (Figure S7a) with an exposed (012) crystal plane can coordinate with the oxygen of PEO to form localized amorphous regions in the vicinity of LZP particles, which reduces the association between Li^+ in the polymer and the oxygen of PEO. This phenomenon results in fast ionic conduction of lithium at the LZP/polymer interface by breaking the weak transient Li^+-O_{PEO} bonds, which adds a new contribution to the overall ionic conductivity of the composite along with the low activation energy of the NASICON LZP (0.4 eV)[43] and the transport channel in the bulk ceramic for fast Li^+ conduction in the (012) plane (Figure S7b).

The Li^+ transport pathway in the CPE(10:1)−25LZP composite was determined with $^6Li \rightarrow {}^7Li$ tracer-exchange NMR[23] on a CPE(10:1)−25LZP membrane that was cycled in a ^6Li/CPE(10:1)−25LZP/^6Li symmetric cell for 100 h. Figure 2c shows ^6Li ions preferentially transport through the disordered Li^+ environment (A2; the mobile Li^+) as the ^6Li signal is enriched by 6.4%, whereas the right peak (A1; the Li^+ closely bound to EO units in PEO) decreases from 39.8% to 33.4%. When the $^6Li \rightarrow {}^7Li$ tracer-exchange NMR is performed at 40 °C, the fraction of mobile Li^+ (A2) is further enriched by ^6Li. The intensity variation between the two ^6Li signals (A1 and A2) indicates that the disordered Li^+ local environment (A2) is prone to ^6Li-enrichment; thus showing that occupation of the disordered A2 is beneficial for ionic conductivity. The ^6Li MAS NMR spectra were acquired twice in a row within a time frame of 12 h. The ^6Li line shape of both acquisitions are identical (Figure S6c). This similarity in line shape rules out the possibility of chemical exchange between A1 and A2. More importantly, this result holds true when the CPE(10:1)−25LZP is polarized with biased potential; otherwise, the intensity of A1 and A2 peaks would have gradually equalized and merged. As a result, Li^+ does not migrate between environments (i.e., A1 ↔ A2) and the ion transport through the membrane is primarily attributed to the movement of Li^+ in A2. Furthermore, the Li^+ mobility is sensitive to the fractions among all Li^+ environments. Cycling $P(EO)_{10}$−LiTFSI−25LZP with ^6Li metals at 40 °C results in a slight increase in ^7Li T_1 time from 0.38 to 0.43 s, while the ^7Li T_1 time (0.40 s) stays almost the same when the $^6Li \rightarrow {}^7Li$ tracer-exchange is executed at room temperature.

Symmetric Li/Li Cell and the Li/CPE−LZP Interface. A symmetric Li/CPE−25LZP/Li cell was cycled to evaluate the compatibility of the composite membrane with a metallic lithium anode and to check whether the composite membrane can suppress lithium-dendrite formation. The impedance plots of the symmetric Li/CPE−25LZP/Li cell and the cell after 100 cycles at 40 °C are shown in Figure 3a; the Li/CPE−25LZP

https://dx.doi.org/10.1021/jacs.9b12233
J. Am. Chem. Soc. 2020, 142, 2497−2505

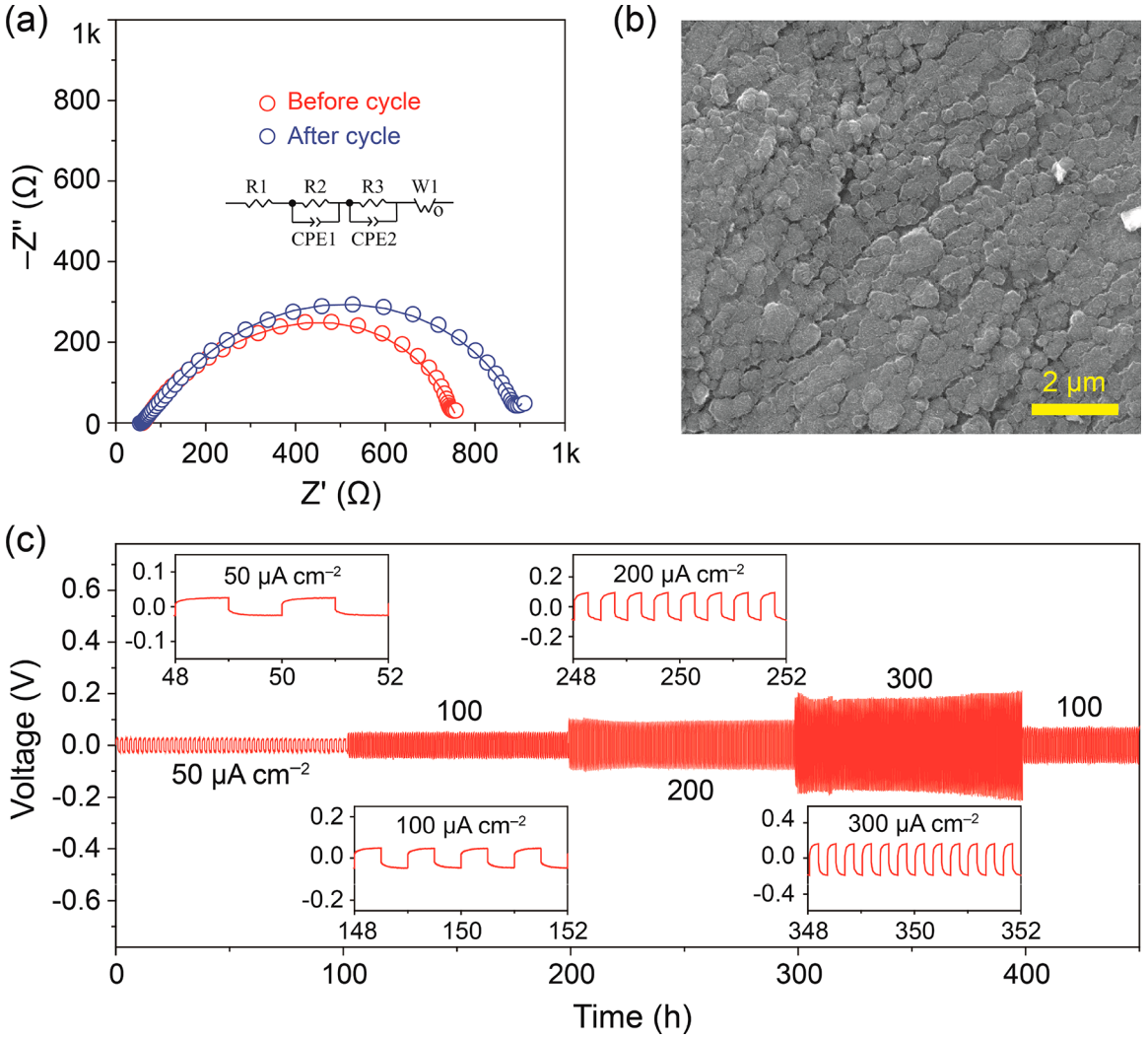

Figure 3. Symmetric Li/Li cell (the areas of Li and CPE (10:1)−25LZP were 0.50 and 0.79 cm^2, respectively). (a) Impedance plots of the Li/Li cell before and after cycling at 40 °C. (b) SEM of lithium metal surface after 100 cycles. (c) Galvanostatic cycling at 40 °C of a Li/Li symmetric cell at different current densities.

interfacial resistances before and after cycling the cell were 175 and 208 Ω cm^2, respectively. Compared with values found in the literature (Table S3), the small Li/CPE−25LZP interfacial resistance reduces the temperature necessary for cycling the cells. The symmetric cell showed a stable cycling from 0.05 to 0.3 mA cm^{-2} (Figure 3c) for 400 h with a small overpotential. The charge/discharge curves of Li/CPE−25LZP/Li and Li/CPE−15Al_2O_3/Li at 0.05 and 0.1 mA cm^{-2} are shown in Figure S8. Variations in the voltage of Li/CPE−25LZP/Li cell during charge and discharge were much smaller than those of the Li/CPE−15Al_2O_3/Li cell because the larger Li^+ transference number of the CPE−25LZP membrane than that of CPE−15Al_2O_3 reduced the concentration overpotential during battery cycling. Micrometer-sized lithium particles formed on the surface of lithium metal during charge (Figure 3b); the symmetric Li/PEO−LiTFSI/Li cell was short-circuited at 0.1 mA cm^{-2} after a short time (Figure S9). PEO is unstable against a Li-metal anode; however, the in situ formed solid electrolyte interphase (SEI) layer containing LiF, Li_3N, and Li_2CO_3 related compounds stabilizes the Li/PEO interface.[44] The introduction of LZP increases the ability of the polymer to suppress lithium-dendrite formation and growth to provide a symmetric cell with a long cycle life.

The color of the surface of the CPE−15Al_2O_3 membrane after cycling the symmetric cell did not change; however, the CPE−25LZP surface color became black after cycling (Figure S10). Previous experiments have shown that lithium metal reacts with a $LiZr_2(PO_4)_3$ pellet to form Li_3P and Li_8ZrO_6 at high temperatures.[32] In an attempt to investigate the chemical composition of the Li-metal/composite polymer interface, we employed time-of-flight secondary ion mass spectrometry (TOF−SIMS), which is a highly sensitive surface and elemental technique.[45,46] Both depth profiling and cross-sectional imaging via TOF-SIMS were employed to probe the Li/solid electrolyte interface (Figure 4). Intrinsic to the TOF−SIMS technique, there is strong fragmentation of all compounds that are sputtered. For instance, $LiZr_2(PO_4)_3$ can only yield fragments that contain a maximum one Li atom, while Li_8ZrO_6 fragments could contain more than one Li atom. Thus, $Li_2ZrO_4^-$ can only originate from Li_8ZrO_6 since it contains more than one Li atom per formula unit. Following this reasoning, we argue that $CsLi_2P^-$ must originate from a Cs combination with Li_3P and not with $LiZr_2(PO_4)_3$ as it contains more than one Li atom. Since the Li_2P^- secondary ion signal was highly suppressed owing to the electropositive nature of Li, we took advantage of the Cs^+ sputtering ion beam for ablating

https://dx.doi.org/10.1021/jacs.9b12233
J. Am. Chem. Soc. 2020, 142, 2497−2505

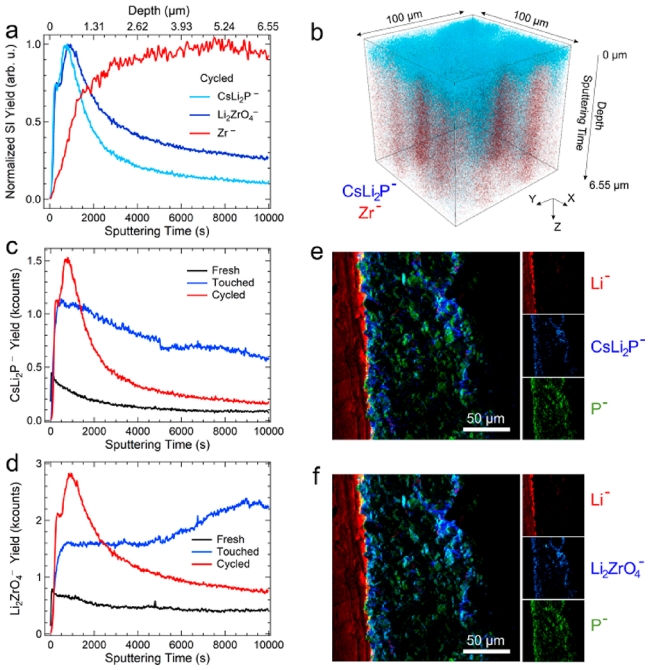

Figure 4. TOF−SIMS of Li/CPE−25LZP interface after cycling the Li/Li cell. (a) Normalized TOF−SIMS depth profiles of three species of interest, $CsLi_2P^-$, $Li_2ZrO_4^-$, and Zr^-, representing the Li_3P and Li_8ZrO_6 reacted species, and bulk $LiZr_2(PO_4)_3$, respectively. (b) Three-dimensional view of the sputtered volume in panel a. Only $CsLi_2P^-$ and Zr^- are shown for clarity. (c, d) Direct comparison between the $CsLi_2P^-$ and $Li_2ZrO_4^-$. Depth profiles obtained from the cycled, touched, and fresh samples. (e, f) TOF−SIMS high lateral resolution secondary ion maps of a Li/solid electrolyte cross-section.

the surface during depth profiling; the Cs^+ forms CsM species, where M is a molecular fragment, in this case Li_2P, due to the interaction between Cs and the surface. Figure 4a demonstrates the surface localization of the $CsLi_2P^-$ and $Li_2ZrO_4^-$ species, where Zr^- was selected as a marker for the bulk solid electrolyte after cycling the Li/Li symmetric cell. The 3D rendering of the sputtered volume shows the spatial distribution of the $CsLi_2P^-$ and Zr^- signals (Figure 4b). Besides the $CsLi_2P^-$ surface localization, we note the slightly discontinuous distribution of both $CsLi_2P^-$ and Zr^-, a result of the particle-like consistency of the solid electrolyte. The $CsLi_2P^-$ and $Li_2ZrO_4^-$ depth profiles are directly compared in Figure 4c,d for the fresh composite membrane, the composite membrane after contact with lithium metal, and the composite membrane after cycling the Li/Li symmetric cell. Both $CsLi_2P^-$ and $Li_2ZrO_4^-$ appear with a significantly higher concentration at the surface of the cycled and touched samples in contrast to the fresh sample. To directly visualize the chemical composition across the Li/solid electrolyte interface, we performed high lateral resolution mapping of this interface in cross-section (Figure 4e,f). These maps provide a clear indication of $CsLi_2P^-$ and $Li_2ZrO_4^-$ localization at the interface and confirm the micrometer-sized, particle-like consistency of the solid electrolyte. Here, the P^- secondary-ion signal was selected as a marker for the bulk of the solid electrolyte owing to the weakness of the Zr^- signal. Both $Li_2ZrO_4^-$ and $CsLi_2P^-$ are sputtered off of the surface of the composite electrolyte as they are representative of the Li_8ZrO_6 and Li_3P components of the SEI formed during cycling. $LiZr_2(PO_4)_3$ reacts with the metallic lithium anode to form an interphase layer composed of Li_8ZrO_6 and Li_3P.[32] This interphase layer increases the wettability of the composite electrolyte by the metallic lithium anode and reduces the contact resistance between the electrodes and polymer electrolyte. This layer serves as a mediating interphase that prevents further interfacial reactions between the electrodes and polymer electrolytes to build a stable solid structure, enabling stable cycling. Li_3P in the interphase is also a good Li^+ conductor,[32] which supplements Li^+ transfer through the interphase.

The All-Solid-State Li-Metal Batteries with CPE−LZP Membrane. All-solid-state Li-metal batteries with the CPE−

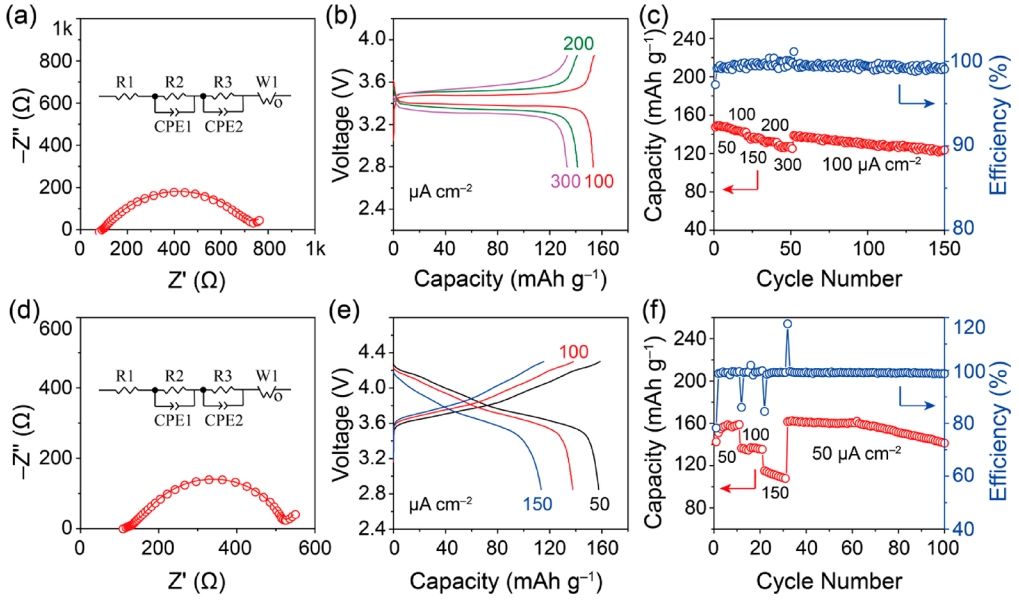

Figure 5. All-solid-state $Li/LiFePO_4$ cell at 40 °C: (a) Electrochemical impedance plots, (b) charge/discharge voltage profiles, and (c) capacity retention and cycling efficiency. All-solid-state Li/NMC cells at 40 °C: (d) Electrochemical impedance plots, (e) charge/discharge voltage profiles, and (f) capacity retention and cycling efficiency. The areas of cathodes, Li, and CPE (10:1)−25LZP were 0.30, 0.50, and 0.79 cm^2, respectively.

https://dx.doi.org/10.1021/jacs.9b12233
J. Am. Chem. Soc. 2020, 142, 2497−2505

25LZP electrolyte and different cathodes ($LiFePO_4$ and $LiNi_{0.8}Mn_{0.1}Co_{0.1}O_2$ (NMC)) were assembled to investigate Li^+ transfer across the CPE−25LZP/cathode interface and the stability of CPE−25LZP membrane in different all-solid-state Li-metal batteries. The linear sweep voltammetry of the Li/CPE−25LZP/stainless steel cell in Figure 1c showed that LZP increased the electrochemical stability of the polymer at voltages above 4 V. The all-solid-state $Li/LiFePO_4$ battery has a total resistance and a CPE−25LZP/$LiFePO_4$ interfacial resistance of 740 Ω and 100 Ω cm^2, respectively, at 40 °C (Figure 5a). The CPE−25LZP electrolyte showed a much smaller interfacial resistance with $LiFePO_4$ cathode than the composite electrolyte with Al_2O_3 as a filler (Table S3).[47] The Li/CPE−25LZP/$LiFePO_4$ cell showed a small overpotential of 0.15 and 0.3 V with a discharge capacity of 155 and 130 mAh g^{-1} at 100 and 300 $\mu A\ cm^{-2}$, respectively (Figure 5b); a discharge capacity of 120 mAh g^{-1} was obtained at 100 $\mu A\ cm^{-2}$ after 150 cycles, and the high Coulombic efficiency above 99% (Figure 5c) indicated a good stability of the CPE−25LZP membrane in the battery. Because the PEO needed as a binder in the cathode is oxidized at voltages above 4.0 V, we used poly(vinylidene fluoride) (PVDF) as the binder in the high-voltage $LiNi_{0.8}Mn_{0.1}Co_{0.1}O_2$ (NMC) cathode to prepare Li/CPE−25LZP/NMC cells. A PVDF−LiTFSI membrane prepared by the same method as that of PEO−LiTFSI membrane showed a Li^+ conductivity of 1.8×10^{-5} S cm^{-1} at 40 °C, but it was stable at voltages above 4.8 V (Figure S12). The composite cathode has an electronic conductivity of 3.2×10^{-5} S cm^{-1} at 40 °C, which is owing to the conductive carbon (Figure S12b). The NMC particles were uniformly coated by the PVDF polymer (Figure S13), and the PEO in the CPE−25LZP was stable at voltages below 4.5 V with the electronic insulating PVDF layer. The Li/CPE−25LZP/NMC cell has a total resistance of 520 Ω at 40 °C (Figure 5d), and the Li/CPE−25LZP/NMC cell showed a typical charge/discharge curve of a NMC cathode from 2.8 to 4.3 V (Figure 5e) with a discharge capacity of 158, 139, and 117 mAh g^{-1} at 50, 100, and 150 $\mu A\ cm^{-2}$, respectively. The cell exhibited good cycling performance with a discharge capacity of 100 mAh g^{-1} after 100 cycles with a Coulombic efficiency of 99.2% (Figure 5f). The contact loss between the cathode active material and PVDF/carbon in the electrode owing to the volume change of the cathode during cycling as well as the possible passivation layer formation at the cathode/PVDF interface may be responsible for the capacity degradation of the cell.[48]

CONCLUSIONS

The use of NASICON $LiZr_2(PO_4)_3$ as a filler in a PEO polymer composite electrolyte has allowed for the investigation of the Li^+ conduction mechanism in this composite type system. Li^+ transfer within the polymer phase dominates the total Li^+ conductivity when the ceramic NASICON particles are isolated within the polymer matrix. However, the interaction between the surface of the LZP particles and the polymer component of the matrix increases the Li^+ transference number and redistributes the Li^+ over two different local environments. A large portion of the Li^+ is reallocated to a disordered local environment (A2) that provides the Li^+ ions greater mobility and improves the conductivity of the polymer composite as a whole. Additionally, the NASICON $LiZr_2(PO_4)_3$ plays a critical role in the in situ formation of an interphase layer between the composite electrolyte and the lithium metal anode. This interphase layer with components from the $LiZr_2(PO_4)_3$ filler increases the ability of the lithium metal anode to wet the composite electrolyte and stabilizes the Li/electrolyte interface, allowing for an all-solid-state Li-metal battery with a long cycle life at a relatively low cycling temperature.

ASSOCIATED CONTENT

Supporting Information

The Supporting Information is available free of charge at https://pubs.acs.org/doi/10.1021/jacs.9b12233.

Synthesis, characterization, and supplementary figures (PDF)

AUTHOR INFORMATION

Corresponding Authors

Yutao Li − *Materials Science and Engineering Program and Texas Materials Institute, The University of Texas at Austin, Austin, Texas 78712, United States;* orcid.org/0000-0003-0798-6880; Email: lytthu@utexas.edu

John B. Goodenough − *Materials Science and Engineering Program and Texas Materials Institute, The University of Texas at Austin, Austin, Texas 78712, United States;* orcid.org/0000-0001-9350-3034; Email: jgoodenough@mail.utexas.edu

Authors

Nan Wu − *Materials Science and Engineering Program and Texas Materials Institute, The University of Texas at Austin, Austin, Texas 78712, United States; Beijing Key Laboratory of Construction Tailorable Advanced Functional Materials and Green Applications, School of Materials Science & Engineering, Beijing Institute of Technology, Beijing 100081, P. R. China;* orcid.org/0000-0003-3100-199X

Po-Hsiu Chien − *Department of Chemistry and Biochemistry, Florida State University, Tallahassee, Florida 32306, United States*

Andrei Dolocan − *Materials Science and Engineering Program and Texas Materials Institute, The University of Texas at Austin, Austin, Texas 78712, United States;* orcid.org/0000-0001-5653-0439

Henghui Xu − *Materials Science and Engineering Program and Texas Materials Institute, The University of Texas at Austin, Austin, Texas 78712, United States;* orcid.org/0000-0003-2790-3122

Biyi Xu − *Materials Science and Engineering Program and Texas Materials Institute, The University of Texas at Austin, Austin, Texas 78712, United States*

Nicholas S. Grundish − *Materials Science and Engineering Program and Texas Materials Institute, The University of Texas at Austin, Austin, Texas 78712, United States*

Haibo Jin − *Beijing Key Laboratory of Construction Tailorable Advanced Functional Materials and Green Applications, School of Materials Science & Engineering, Beijing Institute of Technology, Beijing 100081, P. R. China*

Yan-Yan Hu − *Department of Chemistry and Biochemistry, Florida State University, Tallahassee, Florida 32306, United States;* orcid.org/0000-0003-0677-5897

Complete contact information is available at: https://pubs.acs.org/10.1021/jacs.9b12233

Author Contributions

◇N.W. and P.-H.C. contributed equally.

https://dx.doi.org/10.1021/jacs.9b12233
J. Am. Chem. Soc. 2020, 142, 2497−2505

Notes

The authors declare no competing financial interest.

■ ACKNOWLEDGMENTS

N.W. thanks the China Scholarship Council for the opportunity to work in Texas. This work is supported by the Assistant Secretary for Energy Efficiency and Renewable Energy, Office of Vehicle Technologies, of the U.S. Department of Energy through the Advanced Battery Materials Research (BMR) Program (Battery500 Consortium), award number DE-EE0007762. P.-H.C. and Y.-Y.H. acknowledge the financial support from National Science Foundation under Grant No. DMR-1808517. All solid-sate NMR experiments were performed at the National High Magnetic Field Laboratory. The National High Magnetic Field Laboratory is supported by National Science Foundation through NSF/DMR-1644779 and the State of Florida. Y.L. also acknowledges the funding support from TAFEL UTA18-000175.

■ REFERENCES

(1) Goodenough, J. B.; Park, K.-S. The Li-Ion Rechargeable Battery: A Perspective. *J. Am. Chem. Soc.* **2013**, *135*, 1167−1176.
(2) Manthiram, A.; Yu, X.; Wang, S. Lithium battery chemistries enabled by solid-state electrolytes. *Nat. Rev. Mater.* **2017**, *2*, 16103.
(3) Murugan, R.; Thangadurai, V.; Weppner, W. Fast Lithium Ion Conduction in Garnet-Type $Li_7La_3Zr_2O_{12}$. *Angew. Chem., Int. Ed.* **2007**, *46*, 7778−7781.
(4) Thangadurai, V.; Narayanan, S.; Pinzaru, D. Garnet-type solid-state fast Li ion conductors for Li batteries: critical review. *Chem. Soc. Rev.* **2014**, *43*, 4714−4727.
(5) Li, Y.; Han, J.-T.; Wang, C.-A.; Xie, H.; Goodenough, J. B. Optimizing Li^+ conductivity in a garnet framework. *J. Mater. Chem.* **2012**, *22*, 15357−15361.
(6) Deiseroth, H.-J.; Kong, S.-T.; Eckert, H.; Vannahme, J.; Reiner, C.; Zaiß, T.; Schlosser, M. Li_6PS_5X: A Class of Crystalline Li-Rich Solids With an Unusually High Li^+ Mobility. *Angew. Chem., Int. Ed.* **2008**, *47*, 755−758.
(7) Kamaya, N.; Homma, K.; Yamakawa, Y.; Hirayama, M.; Kanno, R.; Yonemura, M.; Kamiyama, T.; Kato, Y.; Hama, S.; Kawamoto, K.; Mitsui, A. A lithium superionic conductor. *Nat. Mater.* **2011**, *10*, 682.
(8) Kato, Y.; Hori, S.; Saito, T.; Suzuki, K.; Hirayama, M.; Mitsui, A.; Yonemura, M.; Iba, H.; Kanno, R. High-power all-solid-state batteries using sulfide superionic conductors. *Nat. Energy* **2016**, *1*, 16030.
(9) Li, Y.; Chen, X.; Dolocan, A.; Cui, Z.; Xin, S.; Xue, L.; Xu, H.; Park, K.; Goodenough, J. B. Garnet Electrolyte with an Ultralow Interfacial Resistance for Li-Metal Batteries. *J. Am. Chem. Soc.* **2018**, *140*, 6448−6455.
(10) Han, F.; Westover, A. S.; Yue, J.; Fan, X.; Wang, F.; Chi, M.; Leonard, D. N.; Dudney, N. J.; Wang, H.; Wang, C. High electronic conductivity as the origin of lithium dendrite formation within solid electrolytes. *Nat. Energy* **2019**, *4*, 187−196.
(11) Croce, F.; Appetecchi, G. B.; Persi, L.; Scrosati, B. Nanocomposite polymer electrolytes for lithium batteries. *Nature* **1998**, *394*, 456−458.
(12) Wan, J.; Xie, J.; Kong, X.; Liu, Z.; Liu, K.; Shi, F.; Pei, A.; Chen, H.; Chen, W.; Chen, J.; Zhang, X.; Zong, L.; Wang, J.; Chen, L.-Q.; Qin, J.; Cui, Y. Ultrathin, flexible, solid polymer composite electrolyte enabled with aligned nanoporous host for lithium batteries. *Nat. Nanotechnol.* **2019**, *14*, 705−711.
(13) Armand, M. B. Polymer Electrolytes. *Annu. Rev. Mater. Sci.* **1986**, *16*, 245−261.
(14) Sun, C.; Liu, J.; Gong, Y.; Wilkinson, D. P.; Zhang, J. Recent advances in all-solid-state rechargeable lithium batteries. *Nano Energy* **2017**, *33*, 363−386.
(15) Appetecchi, G. B.; Hassoun, J.; Scrosati, B.; Croce, F.; Cassel, F.; Salomon, M. Hot-pressed, solvent-free, nanocomposite, PEO-based electrolyte membranes: II. All solid-state Li/$LiFePO_4$ polymer batteries. *J. Power Sources* **2003**, *124*, 246−253.
(16) Pesko, D. M.; Timachova, K.; Bhattacharya, R.; Smith, M. C.; Villaluenga, I.; Newman, J.; Balsara, N. P. Negative Transference Numbers in Poly(ethyleneoxide)-Based Electrolytes. *J. Electrochem. Soc.* **2017**, *164*, E3569−E3575.
(17) Zheng, Q.; Pesko, D. M.; Savoie, B. M.; Timachova, K.; Hasan, A. L.; Smith, M. C.; Miller, T. F.; Coates, G. W.; Balsara, N. P. Optimizing Ion Transport in Polyether-Based Electrolytes for Lithium Batteries. *Macromolecules* **2018**, *51*, 2847−2858.
(18) Marzantowicz, M.; Dygas, J. R.; Krok, F.; Nowiński, J. L.; Tomaszewska, A.; Florjańczyk, Z.; Zygadło-Monikowska, E. Crystalline phases, morphology and conductivity of PEO:LiTFSI electrolytes in the eutectic region. *J. Power Sources* **2006**, *159*, 420−430.
(19) Marzantowicz, M.; Krok, F.; Dygas, J. R.; Florjańczyk, Z.; Zygadło-Monikowska, E. The influence of phase segregation on properties of semicrystalline PEO:LiTFSI electrolytes. *Solid State Ionics* **2008**, *179*, 1670−1678.
(20) Yang, T.; Zheng, J.; Cheng, Q.; Hu, Y.-Y.; Chan, C. K. Composite Polymer Electrolytes with $Li_7La_3Zr_2O_{12}$ Garnet-Type Nanowires as Ceramic Fillers: Mechanism of Conductivity Enhancement and Role of Doping and Morphology. *ACS Appl. Mater. Interfaces* **2017**, *9*, 21773−21780.
(21) Scrosati, B.; Croce, F.; Persi, L. Impedance Spectroscopy Study of PEO-Based Nanocomposite Polymer Electrolytes. *J. Electrochem. Soc.* **2000**, *147*, 1718−1721.
(22) Liu, W.; Liu, N.; Sun, J.; Hsu, P.-C.; Li, Y.; Lee, H.-W.; Cui, Y. Ionic Conductivity Enhancement of Polymer Electrolytes with Ceramic Nanowire Fillers. *Nano Lett.* **2015**, *15*, 2740−2745.
(23) Zheng, J.; Tang, M.; Hu, Y.-Y. Lithium Ion Pathway within $Li_7La_3Zr_2O_{12}$-Polyethylene Oxide Composite Electrolytes. *Angew. Chem., Int. Ed.* **2016**, *55*, 12538−12542.
(24) Duan, H.; Yin, Y.-X.; Shi, Y.; Wang, P.-F.; Zhang, X.-D.; Yang, C.-P.; Shi, J.-L.; Wen, R.; Guo, Y.-G.; Wan, L.-J. Dendrite-Free Li-Metal Battery Enabled by a Thin Asymmetric Solid Electrolyte with Engineered Layers. *J. Am. Chem. Soc.* **2018**, *140*, 82−85.
(25) Fu, K.; Gong, Y.; Dai, J.; Gong, A.; Han, X.; Yao, Y.; Wang, C.; Wang, Y.; Chen, Y.; Yan, C.; Li, Y.; Wachsman, E. D.; Hu, L. Flexible, solid-state, ion-conducting membrane with 3D garnet nanofiber networks for lithium batteries. *Proc. Natl. Acad. Sci. U. S. A.* **2016**, *113*, 7094−7099.
(26) Liu, W.; Lee, S. W.; Lin, D.; Shi, F.; Wang, S.; Sendek, A. D.; Cui, Y. Enhancing ionic conductivity in composite polymer electrolytes with well-aligned ceramic nanowires. *Nat. Energy* **2017**, *2*, 17035.
(27) Zhai, H.; Xu, P.; Ning, M.; Cheng, Q.; Mandal, J.; Yang, Y. A Flexible Solid Composite Electrolyte with Vertically Aligned and Connected Ion-Conducting Nanoparticles for Lithium Batteries. *Nano Lett.* **2017**, *17*, 3182−3187.
(28) Cheng, L.; Crumlin, E. J.; Chen, W.; Qiao, R.; Hou, H.; Franz Lux, S.; Zorba, V.; Russo, R.; Kostecki, R.; Liu, Z.; Persson, K.; Yang, W.; Cabana, J.; Richardson, T.; Chen, G.; Doeff, M. The origin of high electrolyte-electrode interfacial resistances in lithium cells containing garnet type solid electrolytes. *Phys. Chem. Chem. Phys.* **2014**, *16*, 18294−18300.
(29) Stramare, S.; Thangadurai, V.; Weppner, W. Lithium Lanthanum Titanates: A Review. *Chem. Mater.* **2003**, *15*, 3974−3990.
(30) Chen, L.; Li, Y.; Li, S.-P.; Fan, L.-Z.; Nan, C.-W.; Goodenough, J. B. PEO/garnet composite electrolytes for solid-state lithium batteries: From "ceramic-in-polymer" to "polymer-in-ceramic. *Nano Energy* **2018**, *46*, 176−184.
(31) Zhao, C.-Z.; Zhang, X.-Q.; Cheng, X.-B.; Zhang, R.; Xu, R.; Chen, P.-Y.; Peng, H.-J.; Huang, J.-Q.; Zhang, Q. An anion-immobilized composite electrolyte for dendrite-free lithium metal anodes. *Proc. Natl. Acad. Sci. U. S. A.* **2017**, *114*, 11069.
(32) Li, Y.; Zhou, W.; Chen, X.; Lü, X.; Cui, Z.; Xin, S.; Xue, L.; Jia, Q.; Goodenough, J. B. Mastering the interface for advanced all-solid-state lithium rechargeable batteries. *Proc. Natl. Acad. Sci. U. S. A.* **2016**, *113*, 13313−13317.

https://dx.doi.org/10.1021/jacs.9b12233
J. Am. Chem. Soc. 2020, 142, 2497−2505

(33) Aziz, S. B.; Woo, T. J.; Kadir, M. F. Z.; Ahmed, H. M. A conceptual review on polymer electrolytes and ion transport models. *J. Sci.: Adv. Mater. Devices* **2018**, *3*, 1−17.
(34) Quartarone, E.; Mustarelli, P. Electrolytes for solid-state lithium rechargeable batteries: recent advances and perspectives. *Chem. Soc. Rev.* **2011**, *40*, 2525−2540.
(35) Chen, F.; Yang, D.; Zha, W.; Zhu, B.; Zhang, Y.; Li, J.; Gu, Y.; Shen, Q.; Zhang, L.; Sadoway, D. R. Solid polymer electrolytes incorporating cubic $Li_7La_3Zr_2O_{12}$ for all-solid-state lithium rechargeable batteries. *Electrochim. Acta* **2017**, *258*, 1106−1114.
(36) Wang, C.; Yang, Y.; Liu, X.; Zhong, H.; Xu, H.; Xu, Z.; Shao, H.; Ding, F. Suppression of Lithium Dendrite Formation by Using LAGP-PEO (LiTFSI) Composite Solid Electrolyte and Lithium Metal Anode Modified by PEO (LiTFSI) in All-Solid-State Lithium Batteries. *ACS Appl. Mater. Interfaces* **2017**, *9*, 13694−13702.
(37) Bakker, A.; Gejji, S.; Lindgren, J.; Hermansson, K.; Probst, M. M. Contact ion pair formation and ether oxygen coordination in the polymer electrolytes $M[N(CF_3SO_2)_2]_2PEO_n$ for M = Mg, Ca, Sr and Ba. *Polymer* **1995**, *36*, 4371−4378.
(38) Xue, Z.; He, D.; Xie, X. Poly(ethylene oxide)-based electrolytes for lithium-ion batteries. *J. Mater. Chem. A* **2015**, *3*, 19218−19253.
(39) Zheng, J.; Dang, H.; Feng, X.; Chien, P.-H.; Hu, Y.-Y. Li-ion transport in a representative ceramic-polymer-plasticizer composite electrolyte: $Li_7La_3Zr_2O_{12}$-polyethylene oxide-tetraethylene glycol dimethyl ether. *J. Mater. Chem. A* **2017**, *5*, 18457−18463.
(40) Bloembergen, N.; Purcell, E. M.; Pound, R. V. Relaxation Effects in Nuclear Magnetic Resonance Absorption. *Phys. Rev.* **1948**, *73*, 679−712.
(41) Dai, Y.; Greenbaum, S. G.; Golodnitsky, D.; Ardel, G.; Strauss, E.; Peled, E.; Rosenberg, Y. Lithium-7 NMR studies of concentrated LiI/PEO-based solid electrolytes. *Solid State Ionics* **1998**, *106*, 25−32.
(42) Dai, Y.; Wang, Y.; Greenbaum, S. G.; Bajue, S. A.; Golodnitsky, D.; Ardel, G.; Strauss, E.; Peled, E. Electrical, thermal and NMR investigation of composite solid electrolytes based on PEO, LiI and high surface area inorganic oxides. *Electrochim. Acta* **1998**, *43*, 1557−1561.
(43) Li, Y.; Liu, M.; Liu, K.; Wang, C.-A. High Li^+ conduction in NASICON-type $Li_{1+x}Y_xZr_{2-x}(PO_4)_3$ at room temperature. *J. Power Sources* **2013**, *240*, 50−53.
(44) Xu, H.; Chien, P.-H.; Shi, J.; Li, Y.; Wu, N.; Liu, Y.; Hu, Y.-Y.; Goodenough, J. B. High-performance all-solid-state batteries enabled by salt bonding to perovskite in poly(ethylene oxide). *Proc. Natl. Acad. Sci. U. S. A.* **2019**, *116*, 18815.
(45) Li, W.; Dolocan, A.; Oh, P.; Celio, H.; Park, S.; Cho, J.; Manthiram, A. Dynamic behaviour of interphases and its implication on high-energy-density cathode materials in lithium-ion batteries. *Nat. Commun.* **2017**, *8*, 14589.
(46) Chou, H.; Ismach, A.; Ghosh, R.; Ruoff, R. S.; Dolocan, A. Revealing the planar chemistry of two-dimensional heterostructures at the atomic level. *Nat. Commun.* **2015**, *6*, 7482.
(47) Tan, R.; Gao, R.; Zhao, Y.; Zhang, M.; Xu, J.; Yang, J.; Pan, F. Novel Organic-Inorganic Hybrid Electrolyte to Enable $LiFePO_4$ Quasi-Solid-State Li-Ion Batteries Performed Highly around Room Temperature. *ACS Appl. Mater. Interfaces* **2016**, *8*, 31273−31280.
(48) Koerver, R.; Aygün, I.; Leichtweiß, T.; Dietrich, C.; Zhang, W.; Binder, J. O.; Hartmann, P.; Zeier, W. G.; Janek, J. Capacity Fade in Solid-State Batteries: Interphase Formation and Chemomechanical Processes in Nickel-Rich Layered Oxide Cathodes and Lithium Thiophosphate Solid Electrolytes. *Chem. Mater.* **2017**, *29*, 5574−5582.

https://dx.doi.org/10.1021/jacs.9b12233
J. Am. Chem. Soc. 2020, 142, 2497−2505